



Digital Elevation Models and Orthomosaics of 1989 aerial imagery of the Western Antarctic Peninsula and surrounding islands between 66–68°S

Vijaya Kumar Thota¹, Thorsten Seehaus¹, Friedrich Knuth^{2,3}, Amaury Dehecq⁴, Christian Salewski⁵, David Farías-Barahona⁶, and Matthias H. Braun¹

¹Institut für Geographie, Friedrich-Alexander-Universität Erlangen-Nürnberg, Erlangen, Germany

²Laboratory of Hydraulics, Hydrology and Glaciology (VAW), ETH Zurich, Zurich, Switzerland

³Swiss Federal Institute for Forest, Snow and Landscape Research (WSL),

bâtiment ALPOLE, Sion, Switzerland

⁴Univ. Grenoble Alpes, IRD, CNRS, INRAE, Grenoble INP, IGE, 38000 Grenoble, France

⁵Archiv für deutsche Polarforschung, Alfred-Wegener-Institut, Bremerhaven, Germany

⁶Department of Geography, Universidad de Concepción, Concepción, Chile

Correspondence: Vijaya Kumar Thota (vijaya.kumar.thota@fau.de)

Received: 14 August 2025 – Discussion started: 2 September 2025

Revised: 17 December 2025 – Accepted: 3 January 2026 – Published: 23 January 2026

Abstract. We present a unique, timestamped, high-resolution Digital Elevation Model (DEM) and orthomosaic dataset, derived from aerial imagery that covers about 12 000 km² area on the western Antarctic Peninsula and surrounding islands between 66–68°S. We used a film-based aerial image archive from 1989 acquired by the Institut für Angewandte Geodäsie (IfAG), which is kept in the Archive for German Polar Research at the Alfred Wegener Institute, Germany, to generate the historical DEMs and orthoimages. The reference elevation model of Antarctica (REMA) mosaic is used as a reference DEM to co-register our historical product on stable ground. We evaluated the vertical accuracy of the derived IfAG DEM with independent surface elevation data from ICESat-2 from the summer months of 2020 and 2021. Our historical DEMs have vertical accuracies better than 6 and 8 m with respect to modern elevation data, REMA, and ICESat-2, respectively. The late 20th century DEM and orthomosaic are very valuable observations in a data sparse region, and this dataset will help to quantify historical ice volume changes and inform geodetic mass balance estimates. The dataset is publicly available at <https://doi.org/10.5281/zenodo.17949026> (Thota et al., 2025) and the results presented in this paper are based on version 1.2 of the dataset.

1 Introduction

Monitoring of glaciers dates back to 1830 (Clarke, 1987), when researchers used various instruments, starting from a boulder (fixed marker), stakes, theodolites, and photographs to extract glacier length, area, and volume (mass) changes (Zemp et al., 2015; Oerlemans, 2005). Over time, advancements in remote sensing and imaging technology have expanded glacier monitoring capabilities, thus establishing regional-level monitoring of glaciers for length, area, and volume changes since the early twenty-first century

(Berthier et al., 2016; Braun et al., 2019; Sommer et al., 2020; Hugonnet et al., 2021; Seehaus et al., 2023; The GlaMBIE Team, 2025). The World Glacier Monitoring Service (WGMS) standardizes and provides the mass balance of glaciers available through field measurements (Zemp et al., 2015). However, out of approximately 200000 glaciers worldwide, only 37, mostly in accessible regions like the Alps, have continuous mass balance records dating back to the 20th century (Zemp et al., 2015). Although more glaciers have at least one observation prior to 2000, such historical data remain sparse for the Antarctic Peninsula (AP), a key re-

gion of rapid warming in recent decades (Turner et al., 2016; Oliva et al., 2017; Dussaillant et al., 2025).

The archives of over 30 000 aerial photographs from the Antarctic Peninsula acquired since the 1940s are the only direct observations available over the last century to reconstruct past glacier surface elevations (Fox and Cziferszky, 2008). In 1956–1957, the Falkland Islands and Dependencies Aerial Survey Expedition (FIDASE) undertook extensive aerial mapping surveys throughout the AP. More than 12 000 images were taken along the $\sim 26\,000$ km of ground track (Dodds, 1996; Mott and Wiggins, 1965). Moreover, wide parts of the AP were covered by U.S. aerial surveys in the 1960s. Trimetrogon imagery (a camera system consisting of three cameras, one pointing down, the other two pointed to either side of the flight path at a 30° depression angle) was acquired during these surveys (Dahle et al., 2024). In 1989, the Institut für Angewandte Geodäsie (IfAG) carried out survey flights along the western coast of the AP north of Marguerite Bay near Adelaide Island using the German Research Vessel Polarstern and its helicopters. Large glacierized areas were covered by overlapping vertical photographs. Long-term mass balance analysis from these archives exists for a limited number of glaciers on the Antarctic Peninsula and surrounding Islands. For instance, Kunz et al. (2012) combined various U.S. and U.K. airborne and ASTER space-borne stereo imagery to estimate glacier surface elevation changes for 12 glaciers on the western AP between 1948 and 2010 (primarily 1960s–2005). They revealed a mean near-frontal surface lowering rate of 0.28 ± 0.03 m a $^{-1}$ since the mid-1960s and an increased lowering since the 1990s. Fieber et al. (2016) carried out a case study at Lindblad Cove, north-western AP. They obtained surface elevation change data by combining historical aerial imagery and WorldView-2 satellite stereo-imagery for the period 1957–2014. A total positive mass balance between 0.6 and 5.8 m w.e. was observed throughout the study period. In a follow-up analysis, Fieber et al. (2018) analyzed the surface elevation changes of 16 individual glaciers, grouped at 4 locations on the AP and surrounding islands, between 1956 and 2014. They reported that 81 % of the glaciers exhibited significant thinning, with an average annual mass loss rate of 0.24 ± 0.08 m w.e. Most notably, this was observed at Stadium Glacier, where losses reached up to 62 m w.e. and the glacier front retreated by more than 2.2 km. Dømgaard et al. (2024) reconstructed elevation changes for 21 outlet glaciers across 3 regions of East Antarctica from the 1930s onward, revealing century-scale stability or moderate thickening consistent with long-term snowfall trends. Child et al. (2020) generated the oldest, highest-resolution DEMs for 1 glacier (Byrd Glacier) from aerial photographs taken in the austral summer of 1978, showing largely constant ice-surface elevation over ~ 40 years. So far, the IfAG data has been analyzed only for the San Martín region (McGlary & Northeast glaciers) (Wrobel et al., 2000) and for carrying out a case study at Moider Glacier by Fox and Cziferszky (2008). The results

from the different long-term measurements of glacier surface elevation changes indicate a heterogeneous change pattern and suggest that upscaling of the sparse measurements on regional scales can be significantly biased by the limited availability of data.

Here, we present a unique, timestamped, high-resolution Digital Elevation Model (DEM) and orthomosaic dataset of aerial imagery that covers about $12\,000$ km 2 on the western Antarctic Peninsula and surrounding islands between $66\text{--}68^\circ$ S. The data has been generated with detailed analysis of around 1200 film-based aerial images from 1989 acquired by the Institut für Angewandte Geodäsie (IfAG), Germany, using Multiview Structure from Motion (MV-SfM) methods. The DEMs have been co-registered and evaluated against external elevation data such as the Reference Elevation Model of Antarctica (REMA), ICESat-2 and other historical DEMs (Howat et al., 2019).

2 Data

2.1 IfAG aerial imagery archive

The archive consists of approximately 2000 vertical aerial images, acquired during a photogrammetric survey by the former Institut für Angewandte Geodäsie (IfAG), Frankfurt am Main, Germany (today Federal Agency for Cartography and Geodesy (Bundesamt für Kartographie und Geodäsie - BKG)). The survey covered the areas on the western Antarctic Peninsula near Adelaide Island and the Grandidier Channel between 6 and 20 February 1989. Aerial photographs were taken using a Zeiss RMK A 8.5/23 camera with Agfa Aviphot Pan 200 aerial film at multiple image scales (1 : 70 000, 1 : 30 000, 1 : 15 000, 1 : 10 000, 1 : 5 000) at different locations. Approximately 61 % of the images were acquired at an average flight elevation of 5895 m, yielding a nominal photoscale of 1 : 70 000 with forward overlap of about 60 %. The film positives used here are preserved in the Archive for German Polar Research (Archive für deutsche Polarforschung – AdP) at the Alfred Wegener Institute (AWI) in Bremerhaven, Germany. There, they form part of the aerial image archive of BKG, which is part of the Federal Ministry of the Interior. This collection comprises a total of more than 20 000 images and was donated to the AdP/AWI in 2017 by the BKG together with the necessary rights of use. The films were digitized using a Leica DSW 700 scanner by GTA Geoservice GmbH, Neubrandenburg, Germany. Image positives that are 23 cm \times 23 cm are scanned at an average scanning resolution of $12.5\,\mu\text{m}$ and provided in 8-bit radiometric resolution, resulting in digital images of size $20\,232 \times 18\,829$ (380.948×10^6) pixels (Fig. 1). The average ground sampling distance (GSD) of these images corresponds to 0.875 m. To our knowledge, no scientific publication has extensively used this unique archive to study glacier elevation changes to date.

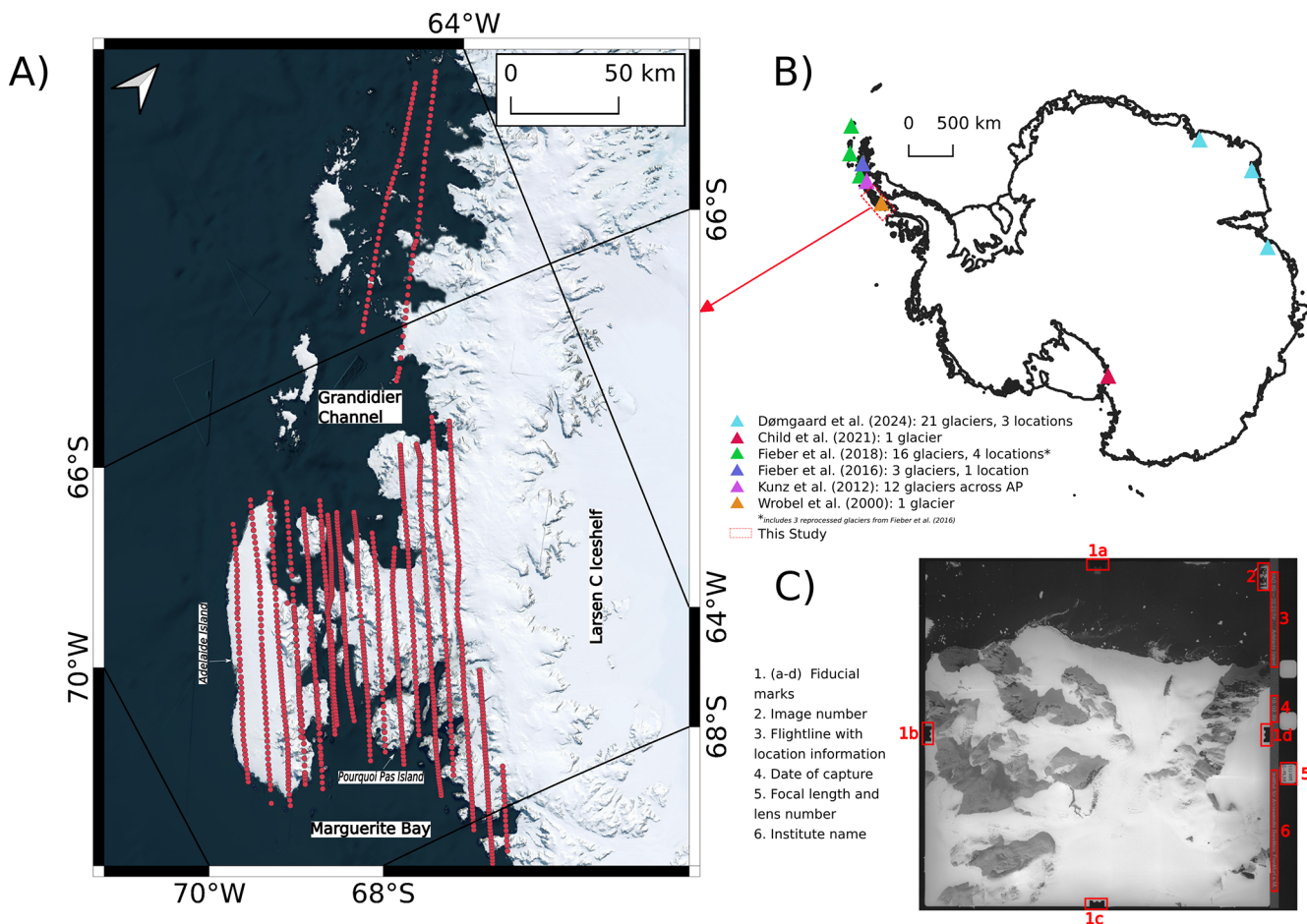


Figure 1. (A) IfAG aerial imagery archive, with red dots representing initial camera locations digitized from survey index map, (B) Antarctic-wide inset map showing the locations of previous studies that explored historical aerial imagery to estimate glacier mass balance and our study area, (C) Scanned IfAG image with metadata information highlighted in red (1–6).

For this study, we selected images from the IfAG dataset that were acquired at a uniform scale of 1 : 70 000. These images were selected due to their consistent coverage and suitability for generating historical DEMs across the study area. Higher-resolution images targeting specific glacier front locations (taken at image scales of 1 : 30 000, 1 : 15 000, 1 : 10 000, and 1 : 5000) are excluded from the analysis, as identifying stable areas for co-registering historical DEMs to modern reference datasets proved challenging at the individual glacier scale.

2.2 Auxiliary data

We used the Reference Elevation Model of Antarctica (REMA, version 2) mosaic as a reference DEM to extract stable (or static) ground elevation for co-registering our historical DEMs derived from the aerial imagery (Howat et al., 2022). The REMA mosaic was downloaded from the Open-Topography portal (<https://portal.opentopography.org/>, last access: 17 December 2025). It is compiled from multiple

REMA strips that are generated using very high resolution (0.32 to 0.5 m) WorldView-1,2,3 and GeoEye-1 satellite imagery through Surface Extraction from TIN-based Searchspace Minimization (SETSM) software (Howat et al., 2019). The mosaic is created to provide a more consistent and complete DEM product with blending and feathering of strip DEMs to avoid edge artefacts. REMA mosaic tiles are co-registered to ICESat-2 and Tandem-X 90 m PolarDEM. Given that REMA is the only high-resolution DEM available with high accuracy, it can be used as an appropriate reference DEM for processing the IfAG data. We used ICESat-2 ATL06 L3A Land Ice Height data from the summer months of 2020 and 2021 to evaluate the vertical accuracy of the derived IfAG DEMs on ice-free areas. Glacier outlines, ice-free areas, and rock outcrops are taken from the Silva et al. (2020) and Antarctic Digital Database (High resolution vector polygons of Antarctic rock outcrop v7.3, Gerrish et al., 2020).

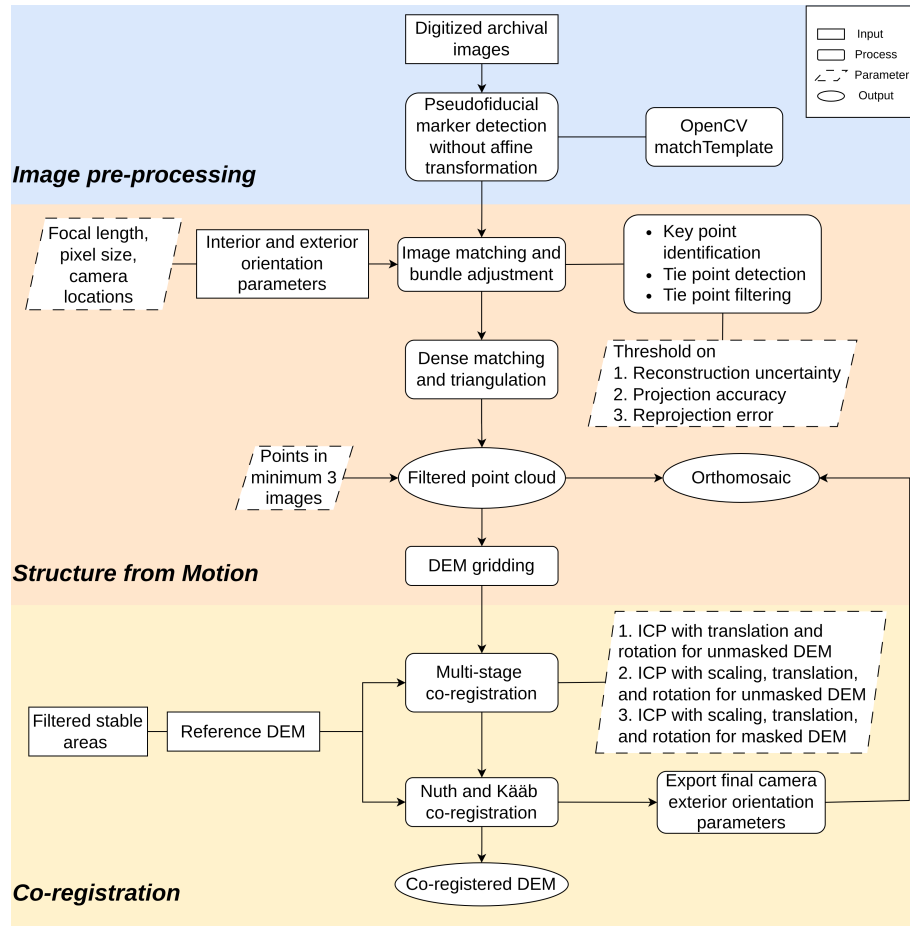


Figure 2. Historical Structure from Motion workflow, adapted from Knuth et al. (2023), ICP = Iterative Closest Point algorithm.

3 Methods

Photogrammetric analysis of our approach is adapted from the Historical Structure from Motion (HSfM) workflow by Knuth et al. (2023) and primarily involves three steps (1) Preparing the scanned imagery for the photogrammetric processing (2) Applying MV-SfM to scanned imagery with estimated camera pose and focal lengths to generate DEMs (3) Multi-stage co-registration of coarsely geolocated DEMs to reference terrain. A detailed description of our approach is provided in the following sections (Fig. 2).

3.1 Camera intrinsics estimation

3.1.1 Fiducial marker detection

The IfAG data comes with pseudofiducial markers (similar to fiducials, but with no clear marker center as opposed to a cross, for example) to secure the interior orientation of the camera (as shown in Fig. 1). These markers serve as reference points for determining the camera's internal geometry at the time of image acquisition. We employed the template matching approach described in Pseudofiducial Marker De-

tection Without Affine Transformation (Knuth et al., 2021b) to automatically detect the locations of each of the four fiducial markers in around 1200 images. The detection algorithm was configured to identify marker positions within a threshold of 40 pixels from the median position of all matches for each fiducial marker, computed per flightline.

The detection results were as follows, for 1193 images, 48.19 % of images had all four fiducial markers detected; 29.50 % of images had three fiducial markers detected; 15.34 % of images had two markers detected; 5.95 % of images had only one marker detected; and 1 % of images had no detectable fiducial markers. The principal point was estimated from fiducial markers that passed quality checks. It was computed as the average of axis-aligned pairwise midpoints (left–right and/or top–bottom). For instances where only two non-opposing markers were detected (e.g. left and bottom), the principal point was estimated using the X coordinate from either the top or bottom marker and the Y coordinate from either the left or right marker (Knuth et al., 2021b). We programmatically estimated the principal point in 93 % of the images. Remaining images with fewer than two fiducials detected, predominantly covering ocean areas

Table 1. Photogrammetric and processing parameters used in Agisoft Metashape for image alignment and dense point cloud generation.

Parameter	Value
Focal Length	85.5 mm
Pixel Size	0.0125 mm
Subsets	8 Numbers – 6 belong to the Mainland: North1, North2, Arrowsmith1, Arrowsmith2, South1, South2. One subset on Adelaide Island, one subset on Pourquoi Pas Island
Alignment Parameters	High quality, 10 000 Tie points, 100 000 Key points, Exclude stationary tie points
Reference Accuracy	Positional ± 1000 m, Yaw 180° , Roll and Pitch $\pm 10^\circ$
Point Cloud Parameters	Medium quality, aggressive filtering
Gridding Resolution	10 m \times 10 m

in flightlines extending outside glaciated areas, were excluded from further analysis. Subsequently, each image was cropped around the principal point to a fixed square dimension corresponding to the metric frame of the Zeiss camera, which has a physical dimension of 226 mm, equivalent to 18 080 pixels (McNabb et al., 2020).

3.1.2 Camera model estimation

The camera calibration reports of the IfAG survey were not found in the AWI archive and were most likely lost before the imagery was transferred to AWI. We therefore estimated unavailable camera intrinsics, i.e., radial and tangential lens distortion parameters, using self-calibration during bundle adjustment performed in Agisoft Metashape (version 2.1.1). To estimate the intrinsic parameters of the single camera used throughout the survey, we performed camera calibration at Pourquoi Pas Island (PPI, see Fig. 3). This site was selected for two main reasons: (1) it contains well-distributed, stable terrain with significant terrain features representative of the broader Antarctic Peninsula, enabling robust parameter estimation despite initial positional inaccuracies (Cziferszky et al., 2010), and (2) it offers the highest image quality in the dataset, with cloud-free coverage and strong visible contrast. We generated a DEM from 27 images from PPI, with initial estimated camera positions (see Sect. 3.2) and focal length of 85.5 mm, iteratively minimizing the residual error with respect to stable area in the REMA strip DEMs from 2019. Using Metashape's default Brown-Conrady lens distortion model (Duane, 1971), we solved for a subset of intrinsic parameters during bundle adjustment, i.e., principal point coordinates (C_x , C_y), as well as radial (K_1 , K_2 , K_3) and tangential (P_1 , P_2) lens distortion coefficients. These final intrinsic camera model parameters derived from PPI were then held fixed and used to process the entire dataset.

3.2 Camera extrinsic estimation

To determine the planimetric information (longitude and latitude) of image centers, we manually estimated their locations using the survey index map from the Institut für Angewandte Geodäsie (IfAG) at a scale of 1 : 500 000, archived at AWI. The map was digitized and georeferenced to establish the initial camera locations. Planimetric coordinates of the image centers are extracted with respect to the WGS84 datum. The approximate elevation of the camera flown at a scale of 1 : 70 000 is 5985 m above ground. We sample the terrain elevation relative to the WGS84 ellipsoid at each initial horizontal location of the camera positions from the REMA mosaic. Therefore, an initial flying height above the ellipsoid (geodetic height) is incorporated as a third dimension into the initial 3D coordinates of the cameras. We input these 3D coordinates with an accuracy estimate of 1000 m to Agisoft Metashape, along with initial Yaw, Pitch, Roll of 0, 0, 0° , with accuracies of 180, 10, 10° , respectively.

3.3 Estimation of Shannon Entropy

We estimated Shannon entropy for each image as an indicator of texture. This metric is used to assess whether variations in DEM coverage were related to image texture and to filter out low-texture images prior to SfM processing. Shannon entropy measures the variability of the data based on the probability of occurrence and is described in Eq. (1):

$$H(X) = - \sum_{i=1}^n p(x_i) \log_2 p(x_i) \quad (1)$$

where $H(X)$ is the entropy of the random variable X and represents the average level of information or uncertainty inherent in the possible outcomes, $p(x_i)$ is the probability of the i th outcome x_i , \log_2 denotes the logarithm base 2, and n is the total number of possible outcomes. The Shannon entropy value ranges from 0 to $\log_x n$, where n is the number of bins (for an 8-bit image is 256) and x is the base. We here used a base of 2, therefore, the range is 0–8 for all of our images.

Table 2. Point cloud quality vs. uncertainty and coverage metrics for PPI subset.

Point Cloud Quality	Image Scale	Points	Filtered Points	Mean Reproj. Error	Elev. Diff. Median (m)	Elev. Diff. NMAD (m)	Coverage (%)	DEM Res (m)
Ultra high	1	335 344 271	105 882 921	0.602	-0.03	1.69	20.60	5
Medium	1/16	48 495 836	28 476 349	0.602	0.06	1.93	44.58	10
Lowest	1/256	4 395 902	3 025 030	0.602	0.31	5.72	71.08	40

3.4 DEM generation

We processed 548 images from 12 flightlines photogrammetrically in Agisoft Metashape version 2.1.1 in 8 different projects (subsets; Fig. 4). The subsets are selected to optimize computational efficiency while encompassing well-distributed stable areas for co-registration, ensuring high absolute accuracy. The Structure from Motion (SfM) workflow is run on a computer with an NVIDIA RTX 500 Ada Generation GPU (32 251 MB, 100 compute units, 2550 MHz) and a CPU AMD Ryzen Threadripper PRO 5955WX 16-Cores 128 GB RAM. All point cloud generation parameters are detailed in Table 1.

Preprocessed images were imported into Metashape, and the tie points were generated at the native resolution of the imagery, facilitating precise and independent alignment of each subset. We set thresholds on quality parameters to reduce the number of incorrect tie points (Over et al., 2021). Initially, we removed all tie points that have a reconstruction uncertainty of more than 10, which is equivalent to a camera base to height ratio of 2.3 (parallax angle of 23°). This removes all points that have a poor viewing angle, which may lead to weak 3D reconstruction and increased uncertainty in depth estimation.

We filtered out tie points with low projection accuracy caused by their poor localization. Tie points are poorly localized when the features they represent are large or less distinct, making it harder to locate their exact position in the images. To remove these points, we applied a projection accuracy threshold of 5, which was measured as the average image scale of the feature across overlapping images. Then, we reduced the reprojection errors of all subsets to less than 0.5 pixels. The filtered tie points were used to estimate the intrinsic and extrinsic camera parameters, which were then applied to generate a dense point cloud for each subset at medium quality, i.e., at a scale sixteen times lower than the original image scale. We selected a medium accuracy in “depth map generation” as a compromise between the required accuracy and coverage (Table 2). To increase the robustness of the generated DEMs, we further excluded the points that were found in fewer than three scenes. We then generated a DEM by gridding the filtered point cloud at 10 m posting in the Antarctic Polar Stereographic (EPSG code 3031) coordinate system. This resolution corresponds to approximately three times the effective GSD of the input images processed at medium quality (originally ~ 3.5 m), thereby minimizing

interpolation artefacts and aligning with the resolution of the 10 m REMA DEM to avoid additional resampling.

3.5 Co-registration

We used the Ames Stereo Pipeline (ASP v3.4)’s *pc_align.py* tool that is embedded in HSFM for multistage co-registration of the generated raw DEMs, based on the Iterative Closest Point (ICP) algorithm (Beyer et al., 2018; Knuth et al., 2023; Shean et al., 2016). At each stage of ICP co-registration, a 12-parameter transformation matrix is calculated according to the expected offset and differences between the reference and raw DEM. In the first step, the rigid body transformation of the point-to-plane algorithm with translation and rotation is applied to the whole raw DEM with respect to the reference DEM (REMA mosaic). In the second step, in addition to translation and rotation, scaling is also added to further converge the offsets to the reference DEM. It is achieved by a similarity-point-to-plane algorithm. The point-to-plane algorithm is more robust to outliers than the point-to-point algorithm and thus converges faster (Li et al., 2020; Shean et al., 2016). In the last stage of ICP co-registration, the alignment is refined by applying translation, rotation, and scaling corrections to stable areas only. Ice-free areas are taken from Silva et al. (2020) and the Antarctic Digital Database (ADD) rock outcrop mask. Stable areas for co-registration are determined by: (1) Filtering these areas to exclude slopes greater than 30° and minimize steep terrain-induced errors. (2) Manually removing blunders in areas where feature matching failed by cross-referencing with the Landsat Image Mosaic of Antarctica (LIMA) and orthoimages (Fig. 3). We set the default expected offset values at each stage of the three-step ICP co-registration procedure to 2500, 500, and 100 m, based on visual inspection of multiple IfAG DEMs. After ICP co-registration, we used Nuth and Kääb (2011) algorithm from the demcoreg package for subpixel co-registration over stable areas, which has a higher accuracy compared to ICP, as demonstrated by a reduction of NMAD after co-registration (Shean et al., 2021). This method estimates and corrects systematic offsets by relating elevation differences to terrain slope and aspect.

Finally, we mosaicked the 6 subsets that belong to the mainland Antarctic Peninsula into one product using the average value of the overlapping area to create a mosaic DEM. We provide DEMs that belong to two islands, i.e., Ade-

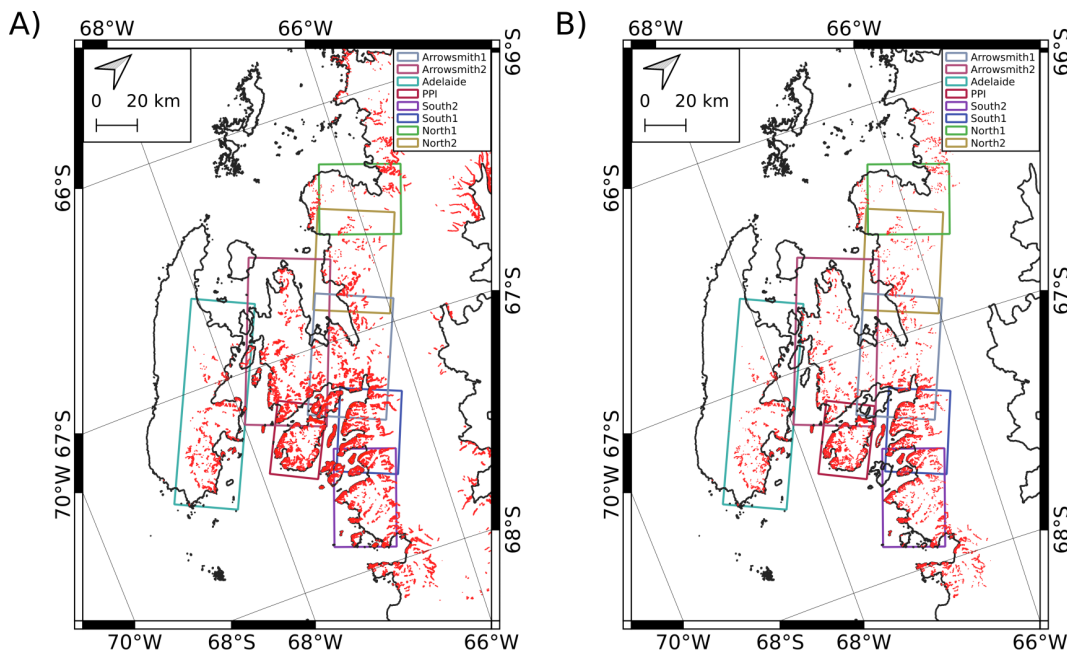


Figure 3. (A) Ice-free areas taken from Silva et al. (2020), (B) Stable areas used for co-registration in our study – slopes $< 30^\circ$ and manually filtered cross-referencing with LIMA and orthoimages, Background- High resolution vector polygons of the Antarctic coastline V7.8 (Gerrish et al., 2023).

laide Island, PPI, as two separate files, along with the pre-coregistration point clouds in eight LAS files. We set the minimum elevation value to 0 and reclassified DEMs to eliminate negative values. We also provide a “bad” pixel mask raster for the mainland DEM, where our DEM is affected due to clouds or artefacts in the reference DEM. We generated this mask by excluding outlier elevation differences with respect to REMA mosaic (values exceeding 4 standard deviations from the mean) within glacier-covered areas, calculated across a binned elevation raster. We suggest using the DEM data where the bad pixel mask raster value is 1.

3.6 Orthoimage generation

The IfAG camera extrinsics are updated by applying the transformation matrix obtained from ICP co-registration and the 3D shift vector from Nuth and Käab (2011) co-registration of IfAG DEMs, and orthomosaics are generated using Metashape at the original resolution. We use Metashape’s void-filling option of the DEMs to generate orthoimages without voids. We provide orthomosaics of 8 subsets in 8 TIFF files.

3.7 Uncertainty estimation

3.7.1 Pixel-level uncertainty

Uncertainties are estimated with two independent datasets, one with the reference DEM used to generate the historical DEMs (REMA mosaic), and the second with the ICESat-

2 data. Uncertainties in the DEMs with respect to REMA are calculated following the approach described by Seehaus et al. (2019). First, elevation offsets (dh) are extracted in ice-free areas, which are then filtered for outliers using 2–98 percentiles of the data. These dh values are binned in 5° slope intervals. Remaining outliers are filtered by applying a 3 times Normalized Median Absolute Deviation (NMAD) filter in each slope bin. Note that these uncertainty estimates relative to REMA include potential errors present in REMA itself (Howat et al., 2019). Therefore, to obtain an independent estimate of vertical accuracy, IfAG DEMs were also compared to ICESat-2. The uncertainty of the IfAG DEMs is assessed using ICESat-2 data by analyzing the distribution of elevation differences between the two datasets over stable areas. We first removed the gross outliers in the offsets by retaining data of less than 50 m offsets, accounting for errors caused by the cloud cover. Subsequently, we applied a 2–98 percentile filter to the entire dataset to exclude extreme values to suppress the impact of processing artefacts. Finally, dh values outside of 3 NMADs were removed across the entire dataset to ensure robust outlier elimination.

3.7.2 Spatially autocorrelated error

We extracted empirical variograms from the elevation difference of IfAG and REMA on ice-free areas to estimate the spatial autocorrelation in our IfAG DEMs. We first standardized the outlier-filtered elevation differences using xDEM’s *infer_heteroscedasticity_from_stable* function, which cap-

Table 3. Percentage of DEM coverage over glacierized and ice-free areas for each subset. Glacier and Ice-free areas are taken from Silva et al. (2020). The table shows the total glacier area and total ice-free area as a percentage of the subset extent, the corresponding DEM coverage percentages on each land class type, the combined total area (Glacier + Ice-free, i.e., excluding ocean), and the overall DEM coverage across both land class types.

Subset	Total Glacier Area (%)	Coverage on Glaciers (%)	Total Ice-free Area (%)	Coverage on Ice-free Area (%)	Total Area (Glacier + Ice-free) (%)	Overall Coverage (Glacier + Ice-free) (%)
North1	74.88	36.98	1.03	40.66	75.91	37.03
North2	79.90	27.92	1.16	69.08	81.06	28.51
Arrowsmith1	77.30	27.53	5.92	56.50	83.22	29.59
Arrowsmith2	56.70	28.95	3.61	54.71	60.31	30.49
South1	62.35	29.69	10.80	55.69	73.15	35.53
South2	61.68	30.84	7.37	66.99	69.05	34.70
PPI	34.45	42.18	10.50	48.57	44.95	43.67
Adelaide Island	52.43	19.51	1.99	29.75	54.42	19.88

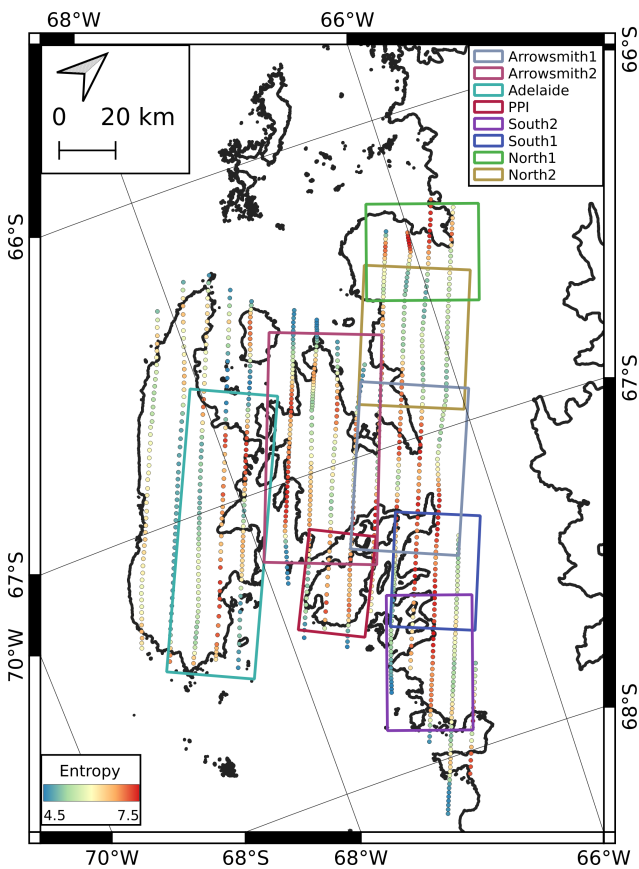


Figure 4. Subsets used in this study overlaid on the Antarctic Coastline. Rectangles represent the eight subsets: six on the Mainland (North1, North2, Arrowsmith1, Arrowsmith2, South1, South2), one on Adelaide Island, and one on Pourquoi Pas Island (PPI). Colored dots indicate the Shannon entropy of individual images (red = high entropy, blue = low entropy). Background- High resolution vector polygons of the Antarctic coastline V7.8 (Gerrish et al., 2023).

tures spatially heteroscedastic variability by estimating elevation error as a function of terrain slope and maximum curvature (xDEM contributors, 2021; Hugonnet et al., 2022). Using a sample size of 5000 from all our standardized elevation differences in ice-free areas, we sampled and averaged 10 unique empirical variograms. We used the *infer_spatial_correlation_from_stable* function in xDEM for this purpose (xDEM contributors, 2021).

4 Results and Discussion

Our processing of the 1989 IfAG aerial imagery archive resulted in three Digital Elevation Models (DEMs) and six orthomosaics covering the mainland Antarctic Peninsula (comprising six subsets: North1, North2, Arrowsmith1, Arrowsmith2, South1, South2) and two for Pourquoi Pas Island (PPI) and Adelaide Island (Figs. 4, 5). In the following sections, we discuss key findings related to the dataset's coverage and image quality, adjustments to camera orientation (exterior and interior), and the vertical accuracy of the DEMs compared to reference datasets (REMA and ICESat-2) and other historical DEMs.

4.1 Image Quality and Coverage

For the IfAG archive, the Shannon entropy value ranged from 4.3 to 7.5, with an average of 6.76 for all selected images (Fig. 4). No scanning-related artefacts are observed in the processed DEMs. Terrain shadows are visible in some places in the South1 subset and may be the cause of 7.18 (high) entropy value in these areas. In Table 3, we summarize the total proportional area and the percentage area coverage of our DEMs of two land classes in our study area 1. Glacier 2. Ice-free areas. We masked our DEMs using the respective layers from Silva et al. (2020). We estimate area coverage percentages by dividing the number of valid pixels in a class by the total pixels of the class. Overall coverage (Glacier + Ice-free Areas) of all DEMs ranges between 20 % and 45 %, with

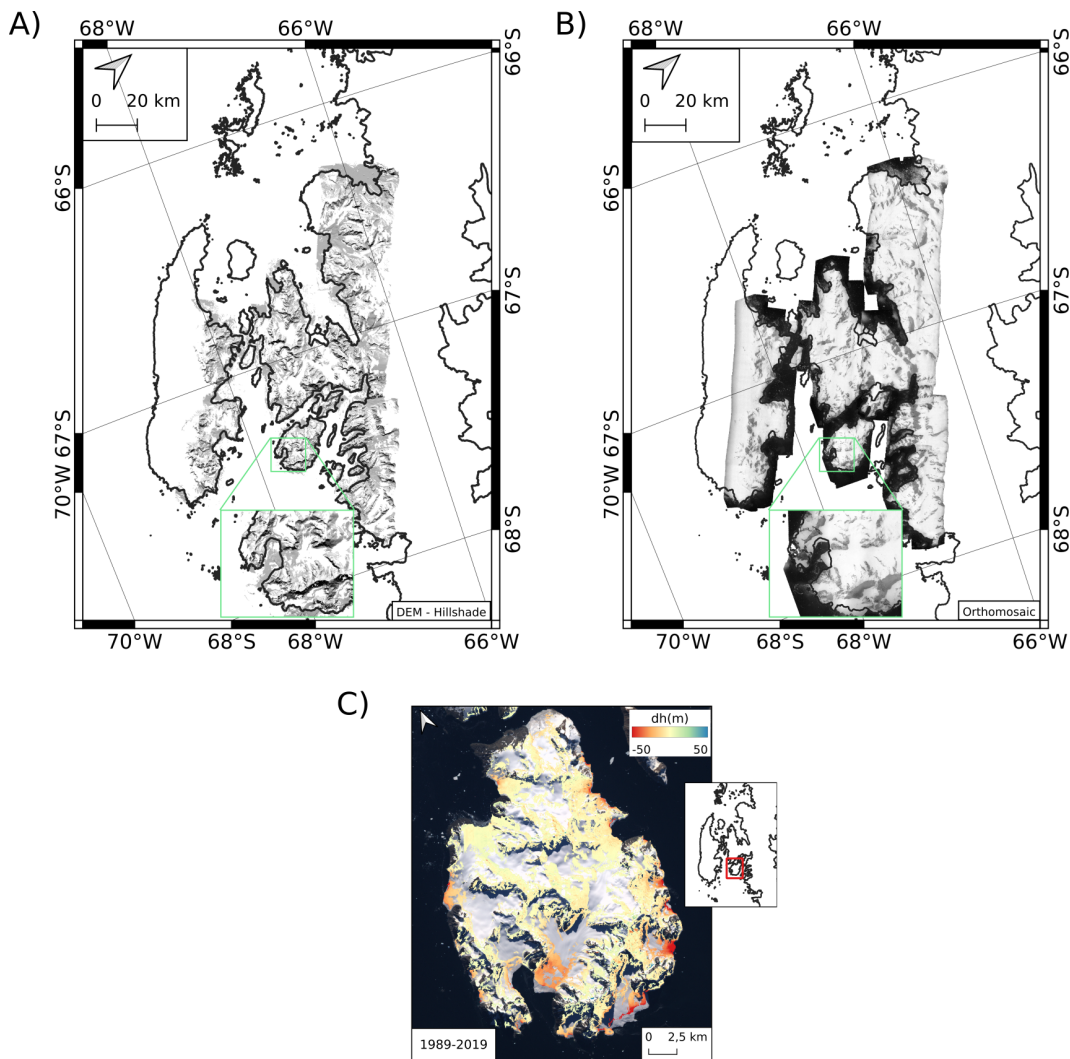


Figure 5. (A) Derived DEMs as hillshade, (B) Orthomosaics, with a background High resolution vector polygons of the Antarctic coastline V7.8 (Gerrish et al., 2023) (C) Decadal elevation change between IfAG DEM from 1989 and a REMA strip DEM from 2019 near PPI with a background LIMA. The gaps in (C) are due to poor coverage of IfAG DEM.

on-glacier coverages spanning 20 %–42 %. We excluded images from the western part of Adelaide Island due to the lack of stable areas and insufficient image features (low entropy; Fig. 4), and from north of Adelaide Island near the Grandi- dier Channel, where images predominantly cover water pixels (Fig. 1). Notably, DEMs for PPI and North1, South1 show higher coverage, which corresponds to the relatively higher average entropy of their source images (Figs. 4, 5).

4.2 Accuracy of Camera Orientation

4.2.1 Accuracy of Exterior Orientation

Exact camera locations and orientations are not available for the IfAG survey. We estimated initial camera positions from the survey index map as mentioned in Sect. 3.2. The accuracy

Table 4. Camera calibration parameters.

Parameter	Value
C_x, C_y	6.1890, -4.4350 (pixels)
K_1	1.706×10^{-5}
K_2	-1.382×10^{-5}
K_3	4.204×10^{-5}
P_1	7.624×10^{-6}
P_2	4.239×10^{-5}

of the generated point clouds and the DEMs depends directly on the accuracy of the camera positions.

The horizontal camera positions were adjusted on average by up to 2000 m during bundle adjustment and an additional

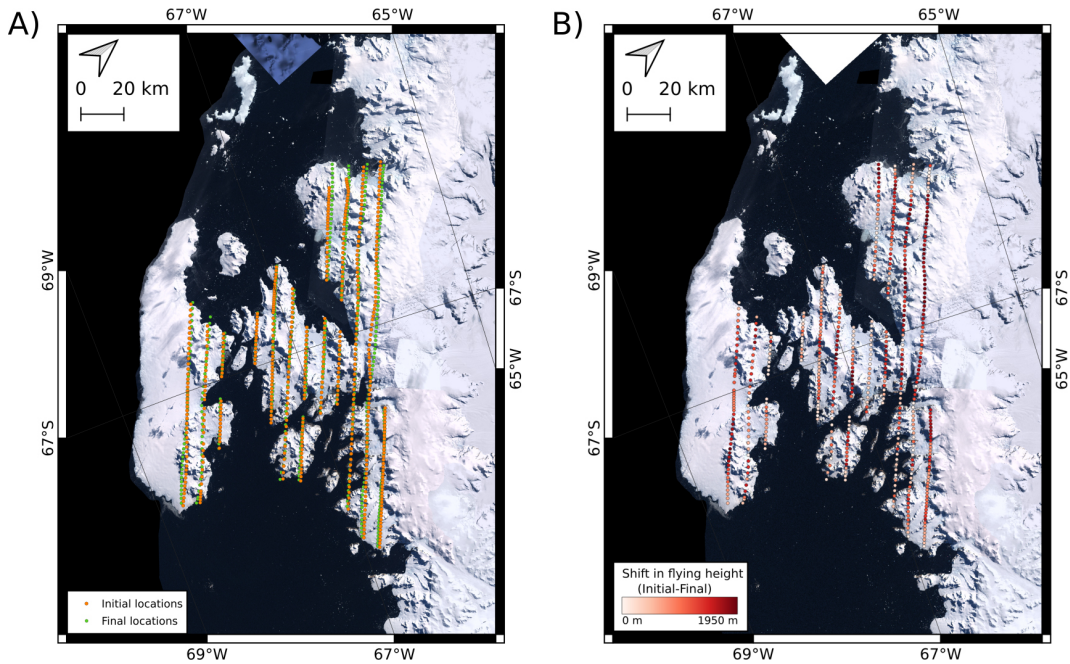


Figure 6. (A) Initial and Final (adjusted) camera locations, (B) Difference in Initial and Final (adjusted) camera flying height, with a background LIMA.

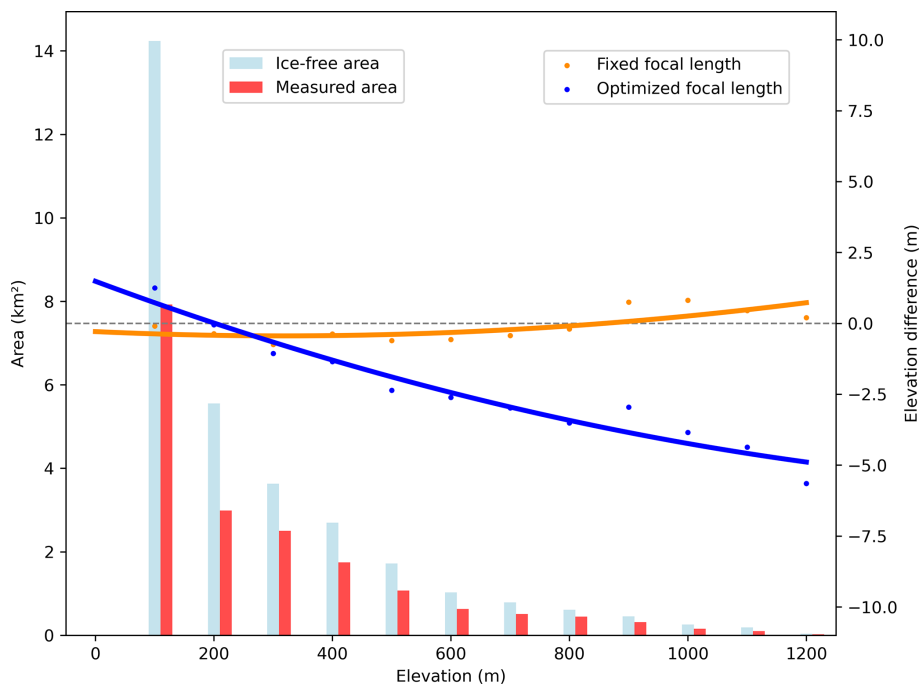


Figure 7. Mean elevation-dependent bias of IfAG DEMs relative to REMA (right y axis), when focal length is fixed (orange) vs. optimized (blue) as a function of altitude bins, lines with respective colors represent a two-degree polynomial fit and ice-free area, measured area, of each bin (left y axis) in light blue, red, respectively.

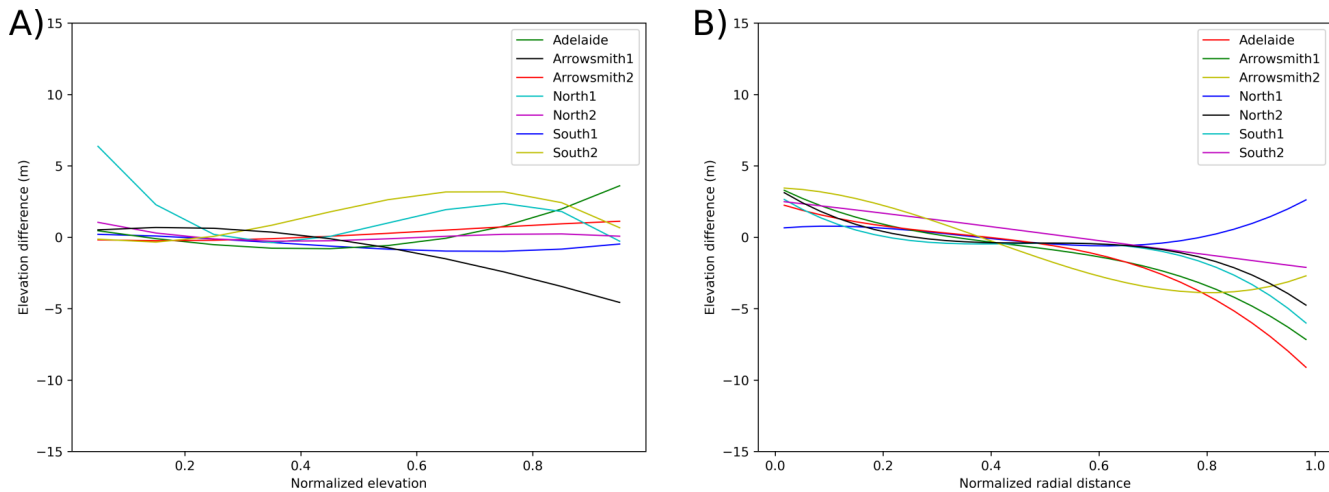


Figure 8. Average elevation bias of IfAG DEMs relative to REMA, with respect to (A) Normalized elevation, (B) Normalized radial distance from subset center.

Table 5. Elevation error statistics for IfAG DEM compared to REMA.

Statistic	0–10°	10–20°	20–30°	> 30°	All Slopes
No. of Observations	160 981	294 415	414 546	3 315 259	4 185 201
Mean (m)	-0.64	-0.39	-0.28	0.51	0.32
Standard Deviation (m)	3.60	3.99	4.51	8.46	7.78
Median (m)	-0.25	-0.22	-0.08	0.60	0.35
NMAD (m)	2.72	3.24	3.98	6.63	5.83

200 m after applying the transform from the co-registration process, while vertical positions were adjusted on average by up to 100 and 50 m, respectively (Fig. 6). Adjustments varied across regions due to differences in terrain, image quality, and flightline overlap. For the mainland subsets, North1 required the largest horizontal adjustments up to 6500 m due to a tightly grouped initial location estimate retrieved from the survey index map (Fig. 6). North2 subset has planimetric camera location corrections up to 2200 m, while South1 and South2 subsets had moderate adjustments of 1200–1800 m. Arrowsmith1 and 2 showed smaller adjustments up to 900–1800 m, benefiting from varying terrain in combination with better image quality. Adelaide Island required horizontal adjustments up to 1800 m, constrained by limited stable areas, while PPI required adjustments of 1200 m. Vertical adjustments followed similar trends, with North1 and North2 requiring up to 80–100 m corrections, while PPI needed only 30–50 m. Applying these corrections improved the accuracy of the point clouds and resulting DEMs, with larger adjustments corresponding to regions that initially had higher uncertainties due to rugged terrain or limited data coverage.

4.2.2 Accuracy of Interior Orientation

We selected the PPI to optimize the unknown interior orientation parameters. The island covers a total of 27 images

Table 6. Elevation error statistics for IfAG DEMs with respect to ICESat-2 data.

Statistic	Mainland	Adelaide Island	PPI
All Slopes			
No. of Observations	4,392	776	619
Mean (m)	0.48	-0.10	0.66
Standard Deviation (m)	8.11	7.63	5.12
Median (m)	0.49	-0.40	0.41
NMAD (m)	7.21	6.86	4.05
Slopes < 30° and Filtered			
No. of Observations	532	217	271
Mean (m)	0.30	-0.43	-0.04
Standard Deviation (m)	5.70	4.45	4.07
Median (m)	0.65	-1.50	-0.04
NMAD (m)	4.16	2.35	2.48

from two flightlines containing high-quality imagery, facilitating robust bundle adjustment in Metashape. We run image alignment in Metashape with an initial extrinsics estimate (Sect. 3.2), a focal length of 85.5 mm, and other processing parameters as mentioned above (Table 1). Allowing the fo-

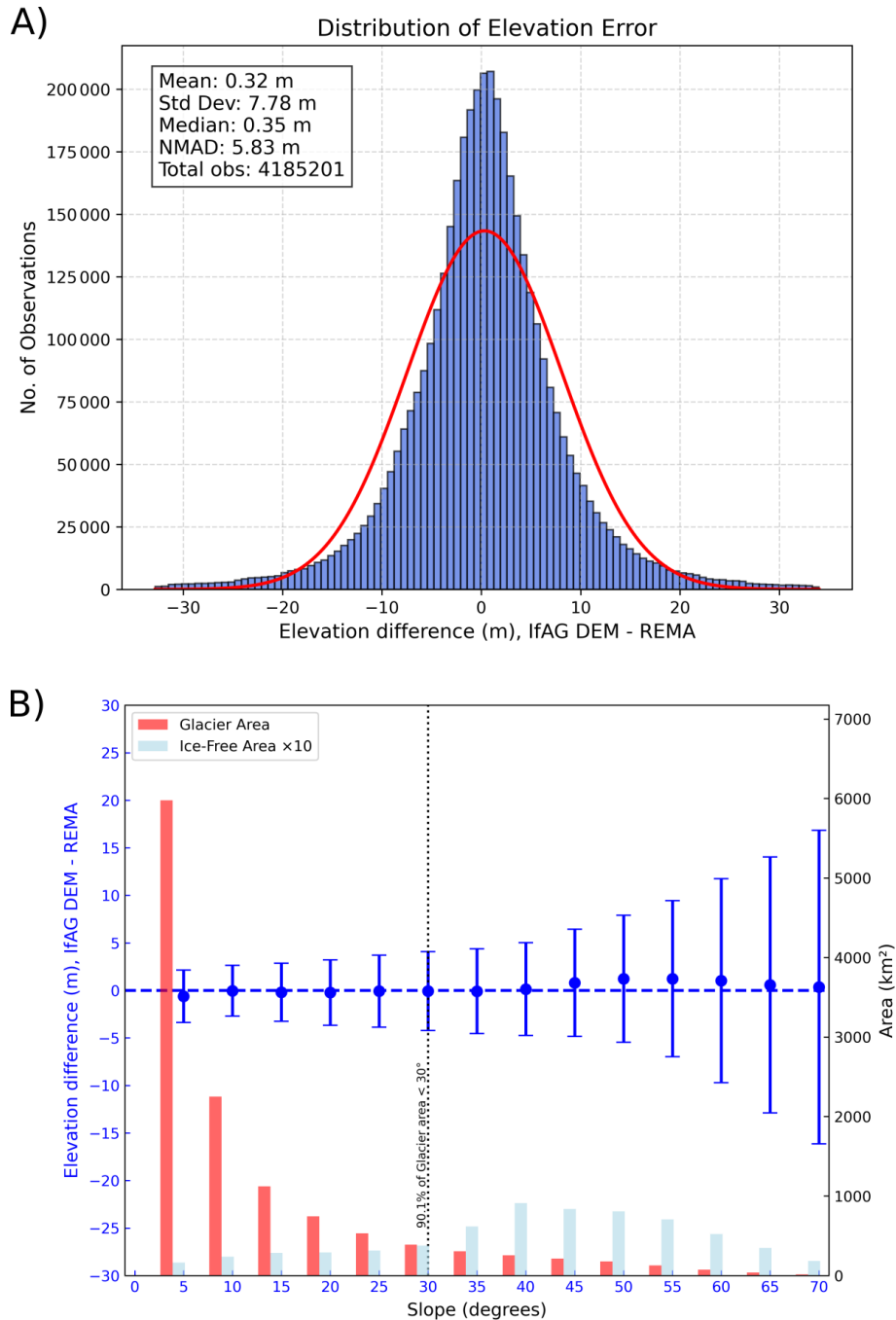


Figure 9. (A) Histograms of elevation difference for IfAG DEMs with REMA, (B) Ice-free (light blue) and Glacier (red) areas and Ice-free area elevation difference (blue dots) distributions as a function of slope, error bars represent NMAD of elevation difference values in the individual slope interval. Note: for better visualisation, Ice-free areas are scaled by a factor of 10.

cal length to be optimized during the bundle adjustment resulted in elevation-dependent biases of up to 5 m, likely due to overfitting in areas with sparse tie points. In contrast, using a fixed focal length reduced these biases (as shown in Fig. 7). Therefore, we adopted a constant focal length throughout the archive.

The estimated camera intrinsic parameters (Table 4), including radial and tangential distortion, were applied to all subsets and regions. The maximum radial distortion associated with these coefficient values was approximately 8 pixels (0.1 mm at image corners), and the maximum tangential distortion was about 1 pixel (0.0125 mm at image corners), indicating well-constrained lens characteristics. Elevation dif-

ferences with respect to the reference DEM on stable areas used for co-registration as a function of normalized elevation and radial distance from each of the subset centers were analyzed to assess the camera model's performance. Across all regions, elevation-dependent biases remained within 5 m, with minimal but consistent biases observed in Arrowsmith1, and South2, where stable areas are limited at higher elevations. For the North1 subset, this bias is pronounced in lower areas too, reflecting the subset-specific challenge of limited availability of stable areas for co-registration in the area. Moreover, biases were most apparent at normalized elevations > 0.6 , reflecting challenges in rugged terrain (Fig. 8). Average elevation bias with respect to normalized radial distance from subset centers showed errors within 5 m except for Arrowsmith1 and Adelaide Island subsets, where biases slightly exceeded 5 m after a normalized radial distance of 0.8. For most of the subsets, higher elevation errors are observed for the pixels farther from the subset center, constrained by the estimated distortion parameters.

4.3 Evaluation of IfAG DEMs with REMA

4.3.1 Pixel-level relative accuracy

We evaluated the accuracy of IfAG DEMs with respect to the reference REMA. DEMs were co-registered to REMA using stable areas with slopes less than 30° . The distribution of elevation differences for our IfAG DEMs on ice-free areas is shown in Fig. 9. The IfAG DEMs have an uncertainty of less than 6 m (NMAD of 5.83 m) with negligible biases on 4 185 201 observations (Table 5). Notably, our DEMs show uncertainty below 5 m for the slopes less than 30° , which is important because only $\sim 10\%$ of the glacier area in the study region is steeper than this slope threshold (Fig. 9). Contrastingly, the uncertainty slightly exceeded 6 m for steeper slopes (NMAD of 6.63 m for slopes $> 30^\circ$). Photogrammetric processing often fails in steep terrain due to shadows and strongly oblique viewing angles, which result in sparse tie points (Nuth and Kääb, 2011). We further observed error variations in different slope categories, with lower slopes showing lower spread in the error and higher slopes showing higher spread, with $0\text{--}10^\circ$, $10\text{--}20^\circ$, $20\text{--}30^\circ$, $> 30^\circ$ slope categories showing NMADs of 2.72, 3.27, 3.98, 6.63 m, respectively (Table 5, Fig. 9). To further characterize the DEM uncertainty, in the following section, we examine the spatial correlation error of the DEM uncertainty.

4.3.2 Spatially autocorrelated error

We fitted a triple-range spherical variogram model to characterize the spatial autocorrelation of elevation error in our IfAG DEMs (Fig. 10). Each nested component represents a distinct contribution, with its sill indicating the proportion of total error variance associated with that spatial scale. The short-range correlation (range of 303.39 m, sill of 0.7969) accounts for the largest share of variance, suggesting that

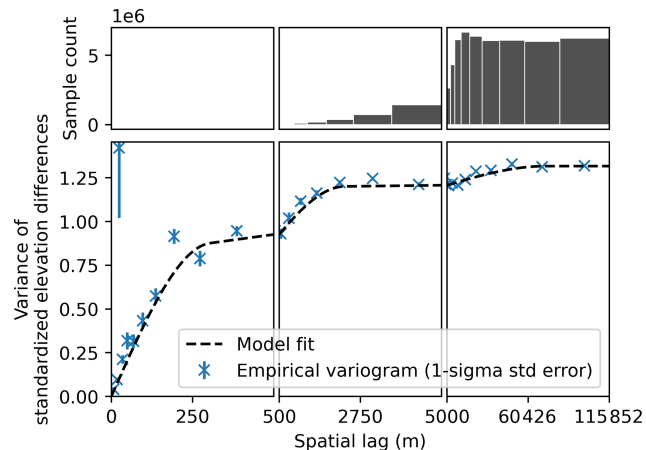


Figure 10. Spatial autocorrelation of elevation error of IfAG compared to REMA. Empirical variograms and triple-range variogram model fit of elevation differences on ice-free areas, Short-range: correlation length of 303.97 m, sill of 0.7969 and Medium-range: correlation length of 2312.29 m, sill of 0.3970 and Long-range: correlation length of 72 606.89 m, sill of 0.1219.

most elevation error arises from local sources such as sensor noise. The medium-range component (range of 2312.29 m, sill of 0.3970) contributes the next major fraction of the variance and likely reflects residual lens distortion that introduces correlated errors over several kilometres (Dehecq et al., 2020). A double-range model failed to capture this substantial medium-scale variance (see Fig. A2), so we used a triple-range spherical model to represent this physically interpretable structure. The smallest proportion of error variance is associated with the long-range correlation (range of 72 606.89 m, sill of 0.1219), which reflects broad regional biases caused by co-registration errors, such as misalignment across image subsets (Dehecq et al., 2020; Hugonnet et al., 2022).

4.4 Evaluation of IfAG DEMs with ICESat-2 data

To evaluate the vertical accuracy of IfAG DEMs with independent surface elevation data, we have taken ICESat-2 ATL06 data from the summers of 2020–2021. Around 70 000 points are available in the ice-free areas in the study area. We estimated the uncertainty with respect to filtered ICESat-2 data on 1. Stable areas used for the co-registration, and 2. All ice-free areas. The ICESat-2 validation dataset was reduced from $\sim 70 000$ to ~ 6000 points after outlier filtering, highlighting the validation challenges in a complex terrain (Table 6, Fig. 11). Our conservative outlier filtering (Sect. 3.7) removed unreliable ICESat-2 data caused by clouds but also highlights misalignment issues with ICESat-2, likely at steep cliffs (further slope filtering reduced the no. of observations to ~ 1000).

All our DEMs have vertical accuracy with respect to ICESat-2 of less than 8 m (maximum NMAD of 7.21 m for

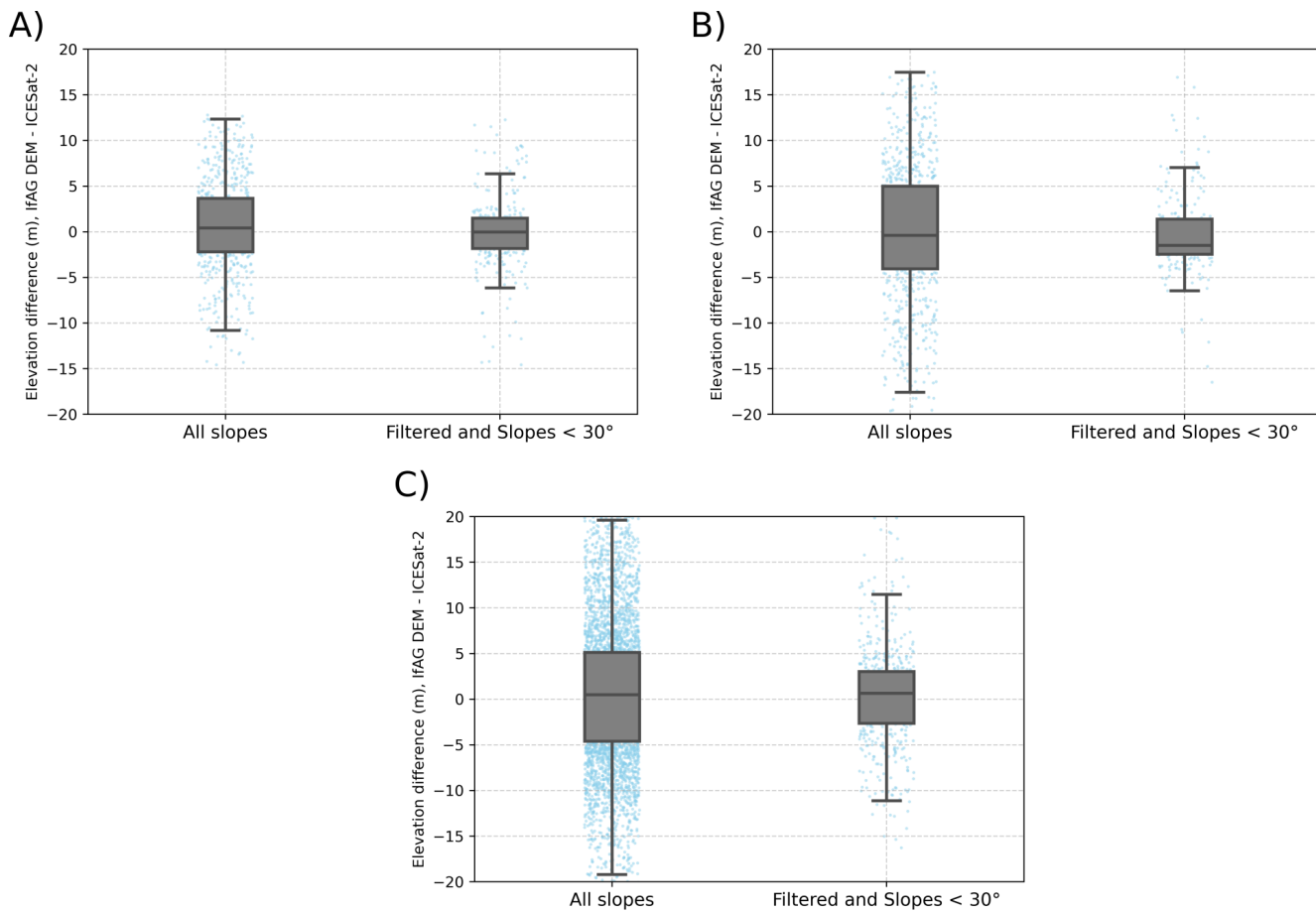


Figure 11. Box plot of elevation change with ICESat-2 for (A) PPI, (B) Adelaide Island, and (C) Mainland DEMs.

Mainland IfAG DEM). A better accuracy of less than 5 m is observed on stable areas used for co-registration (4.16 m for Mainland IfAG DEM). Due to blunders and outliers on slopes greater than 30°, DEMs have biases up to 0.48 m (Mean offset for IfAG mainland mosaic for all slopes). These biases reduce to 0.3 m (Mean offset for IfAG mainland mosaic for filtered, slopes less than 30°), when only lower slopes are considered (Table 6). Furthermore, the accuracy of ICESat-2 is known to degrade at higher curvatures (Shen et al., 2022); the uncertainties of our DEMs may therefore be overestimated in such regions.

4.5 Comparison with other DEMs based on historical aerial imagery

Few DEMs based on similar historical aerial imagery are available for comparison with our IfAG dataset. North and Barrows (2024) recently published an elevation dataset for Larsen B glaciers, derived from 1968 aerial imagery. They reported vertical uncertainties relative to the REMA strip DEMs from 2021 of 15.22 and 19.21 m for Crane and Flask glaciers, respectively. Another dataset covering the Greenland Ice Sheet, based on 1978–1987 aerial imagery,

demonstrated varying vertical accuracies according to the year of the campaign of up to 8.8 m for slopes < 20° and 10.3 m for all slopes when validated against Airborne Topographic Mapper (ATM) data from 1994–2014 (Korsgaard et al., 2016). Fieber et al. (2018) estimated detailed elevation and volume changes of 16 individual glaciers in northern Antarctic Peninsula using FIDASE archives from 1956–1957 austral summers. Using least square surface matching with modern DEMs derived from WorldView-2 imagery, they obtained historical DEMs with post-matching biases varying between +1 to −5.9 m and uncertainties between 7.3 to 28.2 m. In contrast, our IfAG DEMs, derived from 1989 imagery and validated against REMA and ICESat-2 data, exhibit lower vertical uncertainties (e.g., Adelaide Island: NMAD 6.39 m with REMA, Mainland: NMAD 7.21 m with ICESat-2, Fig. A1, Table 6), outperforming the Larsen B datasets by 3–5 times and matching or exceeding the accuracy of the Greenland, northern AP datasets on average.

The larger uncertainties in the Larsen B DEMs may be attributed to the lower quality of the 1968 imagery, poor stereo overlap, manual tie point and GCP placement, and the lack of precise camera positioning. Similarly, the elevated uncertain-

ties in the FIDASE dataset can be attributed to the age and condition of the 1956–1957 film negatives, and differences in type of scanners used in the digital archiving, which led to scaling issues in these image-derived products (Fieber et al., 2016, 2018). Although both the Larsen B and IfAG datasets lack camera calibration reports and rely on imprecise initial camera positions, our DEMs benefit from a refined estimated camera model and an iterative co-registration approach using the Iterative Closest Point (ICP) algorithm. These methods effectively reduce vertical errors, even for subsets with large initial geolocation offsets (up to 6500 m on North1). Additionally, our DEMs show minimal vertical biases relative to REMA (e.g., PPI: −1.22 m, Mainland: 0.49 m, Adelaide Island: 0.82 m, Fig. A1), compared to higher biases reported for Larsen B (e.g., Crane: 6.4 m vs. REMA, −4.16 m vs. ASTER; Flask: −0.06 m vs. REMA, −9.01 m vs. ASTER) (North and Barrows, 2024) and FIDASE (up to −5.9 m vs. WorldView-2) (Fieber et al., 2018). While the Greenland dataset benefits from access to camera calibration reports and extensive terrestrial GPS-based ground control, our comparable accuracies were achieved through the co-registration with and validation against spatially well-distributed reference terrain.

5 Code and data availability

The dataset is publicly available at <https://doi.org/10.5281/zenodo.17949026> (Thota et al., 2025). The Historical Structure from Motion code is publicly available as a Github package with MIT license at <https://doi.org/10.5281/zenodo.5510870> (Knuth et al., 2021a). The aerial images used in this study from the 1989 IfAG survey are open to everyone and can be obtained from the Archive for German Polar Research (Archive für deutsche Polarforschung – AdP) at the Alfred Wegener Institute (AWI) in Bremerhaven, Germany.

6 Conclusions and Outlook

We presented a historical DEM and orthomosaics dataset derived from the IfAG aerial imagery archives from 1989 on the western Antarctic Peninsula and surrounding islands. The dataset has been derived using Multiview Structure from Motion (MV-SfM) methods covering 12 000 km² of glacier area. Using initial camera locations from a survey index map and multistage co-registration based on ICP to a reference DEM (REMA), we processed approximately 550 images to produce a historical elevation dataset. Unavailable camera intrinsic parameters are estimated from 27 images from the calibration site, PPI, and used for the entire mission. With coverage on the glacier surfaces varying between 20 %–42 %, our historical DEMs have vertical accuracies better than 6 and 8 m when compared to modern elevation data, REMA, and ICESat-2, respectively.

Our dataset is a unique product that supports glacier monitoring in one of Earth's most rapidly warming, yet data scarce, regions. Combining our dataset with other historical or modern records could provide an unprecedented multi-temporal long-term analysis of glacier volume, area, and mass changes on the Antarctic Peninsula.

Appendix A: Evaluation of IfAG DEMs with REMA

A1 Pixel-level relative accuracy

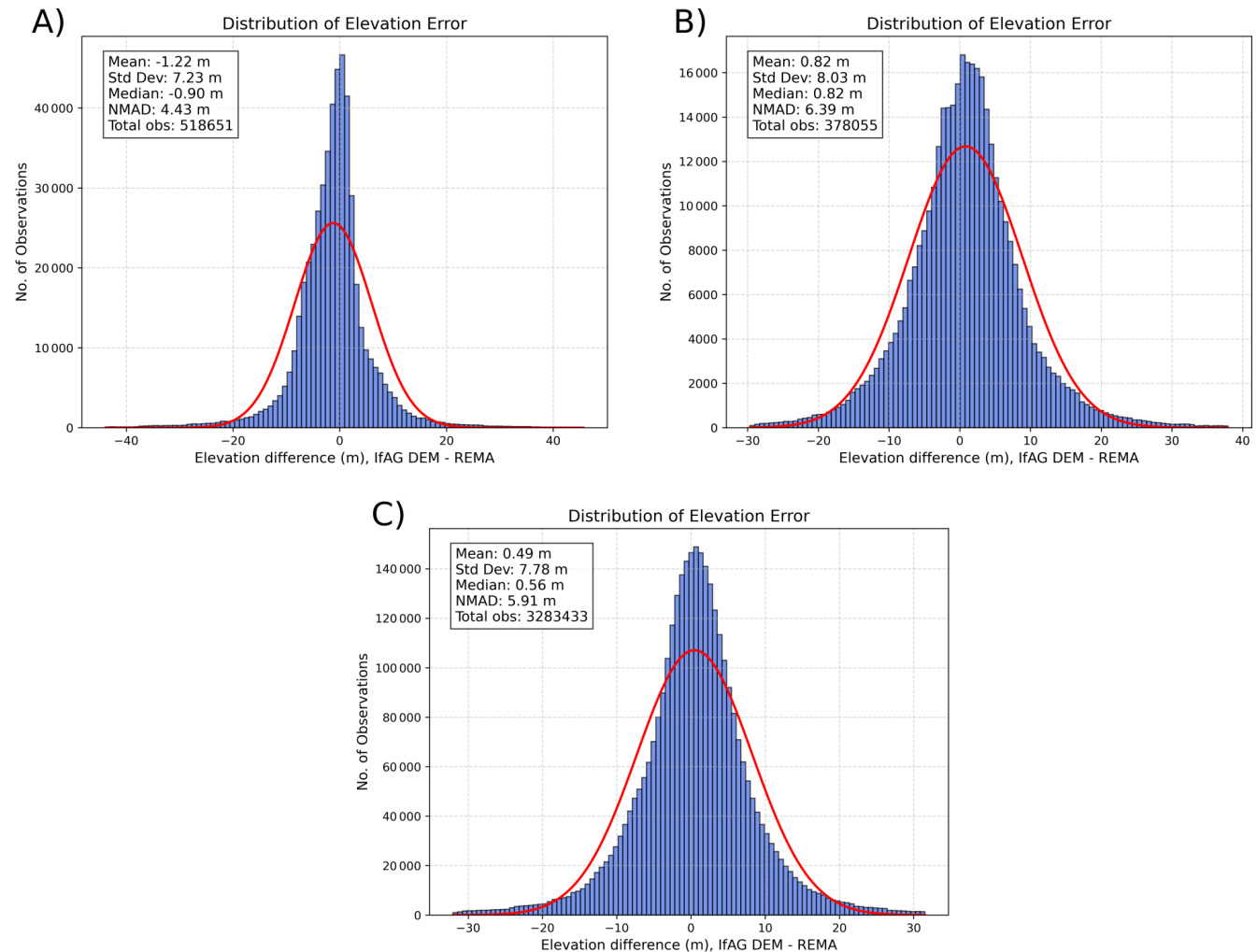


Figure A1. Histograms of elevation difference for IfAG DEMs with REMA on Ice-free areas for (A) PPI, (B) Adelaide Island, and (C) Mainland.

A2 Spatial autocorrelation error

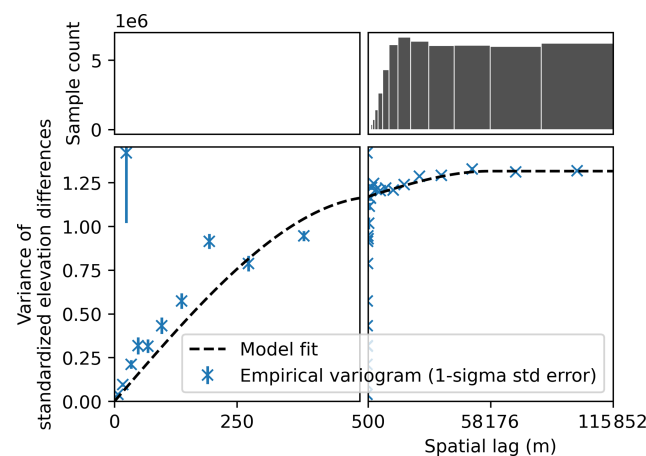


Figure A2. Spatial autocorrelation of elevation error of IfAG compared to REMA. Empirical variograms and double-range variogram model fit of elevation differences on ice-free areas. Short-range: correlation length of 538.24 m, sill of 1.1685 and Long-range: correlation length of 58 155.99 m, sill of 0.1472

Author contributions. VT: Conceptualization, Data Curation, Formal Analysis, Investigation, Methodology, Software, Visualization, Writing – Original Draft Preparation, TS: Conceptualization, Data Curation, Funding Acquisition, Project Administration, Supervision, Writing – Review & Editing. FK: Formal Analysis, Software, Writing – Review & Editing. AD: Formal Analysis, Software, Validation, Writing – Review & Editing. CS: Data curation, Writing – Review & Editing. DB: Conceptualization, Funding Acquisition, Writing – Review & Editing. MB: Conceptualization, Funding Acquisition, Writing – Review & Editing

Competing interests. The contact author has declared that none of the authors has any competing interests.

Disclaimer. Publisher's note: Copernicus Publications remains neutral with regard to jurisdictional claims made in the text, published maps, institutional affiliations, or any other geographical representation in this paper. The authors bear the ultimate responsibility for providing appropriate place names. Views expressed in the text are those of the authors and do not necessarily reflect the views of the publisher.

Acknowledgements. The authors would like to thank the AdP for providing the aerial imagery of the AdP collection F 10: Bunde-samt für Kartographie und Geodäsie (BKG).

To enhance the language and legibility of the manuscript, the authors used ChatGPT (<https://chatgpt.com/>, last access: 17 December 2025) and Grok (<https://grok.com/>, last access: 17 December 2025). The output of this service was reviewed and edited by the authors

as needed. The authors take full responsibility for the content of the presented manuscript.

Financial support. This research has been supported by the European Space Agency (Living Planet Fellowship MIT-AP), the Elitenetzwerk Bayern (grant no. IDP25 M3OCCA), and the Deutsche Forschungsgemeinschaft (DFG) (in the framework of the priority program SPP1158 “Antarctic Research with comparative investigations in Arctic ice areas”, grant no. DFG SE3091/3-1 as well as within the Emmy-Noether-Program, grant no. DFG SE3091/5-1). We acknowledge financial support by Deutsche Forschungsgemeinschaft and Friedrich-Alexander-Universität Erlangen-Nürnberg within the funding programme “Open Access Publication Funding”. Computing resources were partly provided by the project EVERLASTING (Erfassung von Vögeln und Meeressäugetieren in Luftbildsequenzen mittels Verfahren der künstlichen Intelligenz) funded by Bundesamt für Naturschutz (BfN) (grant no. 3523820100).

Review statement. This paper was edited by Katrin Lindbäck and reviewed by Erik Mannerfelt, Felix Dahle, and Shashank Bhushan.

References

- Berthier, E., Cabot, V., Vincent, C., and Six, D.: Decadal region-wide and glacier-wide mass balances derived from multi-temporal ASTER satellite digital elevation models. Validation over the Mont-Blanc area, *Frontiers in Earth Science*, 4, 63, <https://doi.org/10.3389/feart.2016.00063>, 2016.
- Beyer, R. A., Alexandrov, O., and McMichael, S.: The Ames Stereo Pipeline: NASA's Open Source Software for Deriving and Processing Terrain Data, *Earth and Space Science*, 5, 537–548, <https://doi.org/10.1029/2018EA000409>, 2018.
- Braun, M. H., Malz, P., Sommer, C., Farfas-Barahona, D., Sauter, T., Casassa, G., Soruco, A., Skvarca, P., and Seehaus, T. C.: Constraining glacier elevation and mass changes in South America, *Nature Climate Change*, 9, 130–136, 2019.
- Child, S. F., Stearns, L. A., Girod, L., and Brecher, H. H.: Structure-from-motion photogrammetry of antarctic historical aerial photographs in conjunction with ground control derived from satellite data, *Remote Sensing*, 13, 21, <https://doi.org/10.3390/rs13010021>, 2020.
- Clarke, G. K.: Fast glacier flow: Ice streams, surging, and tidewater glaciers, *Journal of Geophysical Research: Solid Earth*, 92, 8835–8841, 1987.
- Cziferszky, A., Fleming, A., and Fox, A.: An assessment of ASTER elevation data over glaciated terrain on Pourquois Pas Island, Antarctic Peninsula, *Geological Society, London, Special Publications*, <https://doi.org/10.1144/SP345>, 2010.
- Dahle, F., Lindenbergh, R., and Wouters, B.: Polar perspectives: a deep dive into geo-referencing historical Antarctic photos, *International Journal of Digital Earth*, 17, 2406384, <https://doi.org/10.1080/17538947.2024.2406384>, 2024.
- Dehecq, A., Gardner, A. S., Alexandrov, O., McMichael, S., Hugonnet, R., Shean, D., and Marty, M.: Automated processing

of declassified KH-9 hexagon satellite images for global elevation change analysis since the 1970s, *Frontiers in Earth Science*, 8, 566802, <https://doi.org/10.3389/feart.2020.566802>, 2020.

Dodds, K.: To Photograph the Antarctic: British Polar Exploration and the Falkland Islands and Dependencies Aerial Survey Expedition (FIDASE), *Ecumene*, 3, 63–89, 1996.

Dømgaard, M., Schomacker, A., Isaksson, E., Millan, R., Huiban, F., Dehecq, A., Fleischer, A., Moholdt, G., Andersen, J. K., and Bjørk, A. A.: Early aerial expedition photos reveal 85 years of glacier growth and stability in East Antarctica, *Nature Communications*, 15, 4466, <https://doi.org/10.1038/s41467-024-48886-x>, 2024.

Duane, C. B.: Close-range camera calibration, *Photogramm. Eng.*, 37, 855–866, 1971.

Dussaillant, I., Hugonnet, R., Huss, M., Berthier, E., Bannwart, J., Paul, F., and Zemp, M.: Annual mass change of the world's glaciers from 1976 to 2024 by temporal downscaling of satellite data with in situ observations, *Earth Syst. Sci. Data*, 17, 1977–2006, <https://doi.org/10.5194/essd-17-1977-2025>, 2025.

Fieber, K., Mills, J., Miller, P., and Fox, A.: Remotely-sensed glacier change estimation: a case study at Lindblad Cove, Antarctic Peninsula, *ISPRS Annals of the Photogrammetry, Remote Sensing and Spatial Information Sciences*, 3, 71–78, 2016.

Fieber, K. D., Mills, J. P., Miller, P. E., Clarke, L., Ireland, L., and Fox, A. J.: Rigorous 3D change determination in Antarctic Peninsula glaciers from stereo WorldView-2 and archival aerial imagery, *Remote Sensing of Environment*, 205, 18–31, 2018.

Fox, A. J. and Cziferszky, A.: Unlocking the time capsule of historic aerial photography to measure changes in Antarctic Peninsula glaciers, *The Photogrammetric Record*, 23, 51–68, 2008.

Gerrish, L., Fretwell, P., and Cooper, P.: High resolution vector polygons of Antarctic rock outcrop (7.3), Cambridge, UK: UK Polar Data Centre, Natural Environment Research Council, UK Research & Innovation [data set], <https://doi.org/10.5285/cbacce42-2fdc-4f06-bdc2-73b6c66aa641>, 2020.

Gerrish, L., Ireland, L., Fretwell, P., and Cooper, P.: High resolution vector polygons of the Antarctic coastline (7.8), BAS Data Catalogue [data set], <https://doi.org/10.5285/c7fe759d-e042-479a-9ecf-274255b4f0a1>, 2023.

Howat, I., Porter, C., Noh, M.-J., Husby, E., Khuvis, S., Danish, E., Tomko, K., Gardiner, J., Negrete, A., Yadav, B., Klassen, J., Kelleher, C., Cloutier, M., Bakker, J., Enos, J., Arnold, G., Bauer, G., and Morin, P.: The Reference Elevation Model of Antarctica – Mosaics, Version 2, Harvard Dataverse [data set], <https://doi.org/10.7910/DVN/EBW8UC>, 2022.

Howat, I. M., Porter, C., Smith, B. E., Noh, M.-J., and Morin, P.: The Reference Elevation Model of Antarctica, *The Cryosphere*, 13, 665–674, <https://doi.org/10.5194/tc-13-665-2019>, 2019.

Hugonnet, R., McNabb, R., Berthier, E., Menounos, B., Nuth, C., Girod, L., Farinotti, D., Huss, M., Dussaillant, I., Brun, F., and Kääb, A.: Accelerated global glacier mass loss in the early twenty-first century, *Nature*, 592, 726–731, 2021.

Hugonnet, R., Brun, F., Berthier, E., Dehecq, A., Mannerfelt, E. S., Eckert, N., and Farinotti, D.: Uncertainty analysis of digital elevation models by spatial inference from stable terrain, *IEEE Journal of Selected Topics in Applied Earth Observations and Remote Sensing*, 15, 6456–6472, 2022.

Knuth, F., Schwat, E., Shean, D., Bhushan, S., and Alexandrov, O.: Historical Structure from Motion (HSfM) pre-release v0.1, Zenodo [code], <https://doi.org/10.5281/zenodo.5510870>, 2021a.

Knuth, F., Schwat, E., Shean, D., and McNeil, C.: Historical Image Pre-Processing (HIPP) pre-release v0.1, Zenodo [code], <https://doi.org/10.5281/zenodo.5510876>, 2021b.

Knuth, F., Shean, D., Bhushan, S., Schwat, E., Alexandrov, O., McNeil, C., Dehecq, A., Florentine, C., and O'Neil, S.: Historical Structure from Motion (HSfM): Automated processing of historical aerial photographs for long-term topographic change analysis, *Remote Sensing of Environment*, 285, 113379, <https://doi.org/10.1016/j.rse.2022.113379>, 2023.

Korsgaard, N. J., Nuth, C., Khan, S. A., Kjeldsen, K. K., Bjørk, A. A., Schomacker, A., and Kjær, K. H.: Digital elevation model and orthophotographs of Greenland based on aerial photographs from 1978–1987, *Scientific Data*, 3, 1–15, 2016.

Kunz, M., King, M. A., Mills, J. P., Miller, P. E., Fox, A. J., Vaughan, D. G., and Marsh, S. H.: Multi-decadal glacier surface lowering in the Antarctic Peninsula, *Geophysical Research Letters*, 39, <https://doi.org/10.1029/2012GL052823>, 2012.

Li, P., Wang, R., Wang, Y., and Tao, W.: Evaluation of the ICP algorithm in 3D point cloud registration, *IEEE Access*, 8, 68030–68048, 2020.

McNabb, R., Girod, L., Nuth, C., and Kääb, A.: An open-source toolset for automated processing of historic spy photos: sPyMicMac, EGU General Assembly 2020, Online, 4–8 May 2020, EGU2020-11150, <https://doi.org/10.5194/egusphere-egu2020-11150>, 2020.

Mott, P. and Wiggins, W.: Falkland Islands and Dependencies Aerial Survey Expedition 1955–57, *The Geographical Journal*, 131, 430–432, 1965.

North, R. and Barrows, T. T.: High-resolution elevation models of Larsen B glaciers extracted from 1960s imagery, *Scientific Reports*, 14, 14536, <https://doi.org/10.1038/s41598-024-65081-6>, 2024.

Nuth, C. and Kääb, A.: Co-registration and bias corrections of satellite elevation data sets for quantifying glacier thickness change, *The Cryosphere*, 5, 271–290, <https://doi.org/10.5194/tc-5-271-2011>, 2011.

Oerlemans, J.: Extracting a climate signal from 169 glacier records, *Science*, 308, 675–677, 2005.

Oliva, M., Navarro, F., Hrbáček, F., Hernández, A., Nývlt, D., Pereira, P., Ruiz-Fernández, J., and Trigo, R.: Recent regional climate cooling on the Antarctic Peninsula and associated impacts on the cryosphere, *Science of the Total Environment*, 580, 210–223, 2017.

Over, J.-S. R., Ritchie, A. C., Kranenburg, C. J., Brown, J. A., Buscombe, D. D., Noble, T., Sherwood, C. R., Warrick, J. A., and Wernette, P. A.: Processing coastal imagery with Agisoft Metashape Professional Edition, version 1.6 – Structure from motion workflow documentation, Tech. rep., US Geological Survey, <https://doi.org/10.3133/ofr20211039>, 2021.

Seehaus, T., Malz, P., Sommer, C., Lippl, S., Cochachin, A., and Braun, M.: Changes of the tropical glaciers throughout Peru between 2000 and 2016 – mass balance and area fluctuations, *The Cryosphere*, 13, 2537–2556, <https://doi.org/10.5194/tc-13-2537-2019>, 2019.

Seehaus, T., Sommer, C., Dethinne, T., and Malz, P.: Mass changes of the northern Antarctic Peninsula Ice Sheet de-

rived from repeat bi-static synthetic aperture radar acquisitions for the period 2013–2017, *The Cryosphere*, 17, 4629–4644, <https://doi.org/10.5194/tc-17-4629-2023>, 2023.

Shean, D., Bhushan, S., Lilien, D., Knuth, F., Schwat, E., Meyer, J., Sharp, M., and Hu, M.: *dshean/demcoreg*: v1.1.0, Zenodo [code], <https://doi.org/10.5281/zenodo.5733347>, 2021.

Shean, D. E., Alexandrov, O., Moratto, Z. M., Smith, B. E., Joughin, I. R., Porter, C., and Morin, P.: An automated, open-source pipeline for mass production of digital elevation models (DEMs) from very-high-resolution commercial stereo satellite imagery, *ISPRS Journal of Photogrammetry and Remote Sensing*, 116, 101–117, 2016.

Shen, X., Ke, C.-Q., Fan, Y., and Drolma, L.: A new digital elevation model (DEM) dataset of the entire Antarctic continent derived from ICESat-2, *Earth Syst. Sci. Data*, 14, 3075–3089, <https://doi.org/10.5194/essd-14-3075-2022>, 2022.

Silva, A. B., Arigony-Neto, J., Braun, M. H., Espinoza, J. M. A., Costi, J., and Jaña, R.: Spatial and temporal analysis of changes in the glaciers of the Antarctic Peninsula, *Global and Planetary Change*, 184, 103079, <https://doi.org/10.1016/j.gloplacha.2019.103079>, 2020.

Sommer, C., Malz, P., Seehaus, T. C., Lippl, S., Zemp, M., and Braun, M. H.: Rapid glacier retreat and downwasting throughout the European Alps in the early 21st century, *Nature Communications*, 11, 3209, <https://doi.org/10.1038/s41467-020-16818-0>, 2020.

The GlaMBIE Team: Community estimate of global glacier mass changes from 2000 to 2023, *Nature*, 1–7, <https://doi.org/10.1038/s41586-024-08545-z>, 2025.

Thota, V. K., Seehaus, T., Knuth, F., Dehecq, A., Salewski, C. R., Farías-Barahona, D., and Braun, M.: Digital Elevation Models and Orthomosaics of Institut für Angewandte Geodäsie (IfAG) Aerial Imagery from 1989, Zenodo [data set], <https://doi.org/10.5281/zenodo.17949026>, 2025.

Turner, J., Lu, H., White, I., King, J. C., Phillips, T., Hosking, J. S., Bracegirdle, T. J., Marshall, G. J., Mulvaney, R., and Deb, P.: Absence of 21st century warming on Antarctic Peninsula consistent with natural variability, *Nature*, 535, 411–415, 2016.

Wrobel, B. P., Walter, H., Friehl, M., Hoppe, U., and Schlüter, M.: A topographical data set of the glacier region at San Martin, Marguerite Bay, Antarctic Peninsula, generated by digital photogrammetry, *Polarforschung*, 67, 53–63, 2000.

xDEM contributors: xDEM, Zenodo [code], <https://doi.org/10.5281/zenodo.4809698>, 2021.

Zemp, M., Frey, H., Gärtner-Roer, I., Nussbaumer, S. U., Hoelzle, M., Paul, F., Haeberli, W., Denzinger, F., Ahlstrøm, A. P., Anderson, B., Bajracharya, S., Baroni, C., Braun, L. N., Cáceres, B. E., Casassa, G., Cobos, G., Dávila, L. R., Delgado Granados, H., Demuth, M. N., Espizua, L., Fischer, A., Fujita, K., Gadek, B., Ghazanfar, A., Hagen, J. O., Holmlund, P., Karimi, N., Li, Z., Pelto, M., Pitte, P., Popovnina, V. V., Portocarrero, C. A., Prinz, R., Sangewar, C. V., Severskiy, I., Sigurðsson, O., Soruco, A., Usualiev, R., and Vincent, C.: Historically unprecedented global glacier decline in the early 21st century, *Journal of Glaciology*, 61, 745–762, 2015.